d-wave superconductivity on the honeycomb bilayer

J. Vučičević,[1] M. O. Goerbig,[2] and M. V. Milovanović[1]

[1]*Scientific Computing Laboratory, Institute of Physics Belgrade, University of Belgrade, Pregrevica 118, 11080 Belgrade, Serbia*

[2]*Laboratoire de Physique des Solides, Université Paris-Sud, CNRS UMR 8502, F-91405 Orsay Cedex, France*

(Received 19 February 2012; revised manuscript received 1 August 2012; published 7 December 2012)

We introduce a microscopic model on the honeycomb bilayer, which in the small-momentum limit captures the usual (quadratic dispersion in the kinetic term) description of bilayer graphene. In the limit of strong interlayer hopping it reduces to an effective honeycomb monolayer model with also third-neighbor hopping. We study interaction effects in this effective model, focusing on possible superconducting instabilities. We find $d_{x^2-y^2}$ superconductivity in the strong-coupling limit of an effective tJ-model-like description that gradually transforms into $d+id$ time-reversal symmetry-breaking superconductivity at weak couplings. In this limit the small-momentum order-parameter expansion is $(k_x+ik_y)^2$ [or $(k_x-ik_y)^2$] in both valleys of the effective low-energy description. The relevance of our model and investigation for the physics of bilayer graphene is also discussed.

DOI: 10.1103/PhysRevB.86.214505 PACS number(s): 74.20.Mn, 74.20.Rp, 74.70.Wz, 73.20.At

I. INTRODUCTION

Interaction effects are expected to be important for the physics of bilayer graphene and may cause a formation of correlated many-body phases.[1,2] This needs to be contrasted to intrinsic monolayer graphene, in which a vanishing density of states at the Dirac points suppresses the influence of electronic correlations.[2,3] Recent experiments on suspended bilayer graphene,[4–7] which is free of substrate effects, reveal a gapped state at and around the charge neutrality point. The state may be of topological origin[8] due to the observed[4,6] conductance of the order of e^2/h and may exhibit an anomalous quantum Hall effect, i.e., a quantum Hall effect at zero magnetic field. In the most recent experiment on high mobility samples, from Ref. 7, a completely insulating behavior was found.

From the theory point of view, several proposals were given[9–19] for the existence of gapped (and gapless) phases at the charge neutrality point, including those that break the time-reversal symmetry. Most of them are based on the particle-hole (excitonic) binding, which is the most natural assumption in the understanding of a gapped phase at the charge neutrality point. These theories assume a quadratic dispersion of the electrons in the low-energy effective description,[20] and direct hopping between two sublattices in different layers that leads to the linear dispersion ("triagonal warping") is neglected. This assumption is justified if the chemical potential is not exactly situated at the charge neutrality point.

To explore additional possibilities for gapped phases in the presence of a finite chemical potential, we discuss here superconducting instabilities, especially with an eye on the possibility of topological (fully gapped) superconductivity on the honeycomb bilayer. Bilayer graphene may be potentially also viewed as a strongly correlated system with a possibility to support a layered antiferromagnetic state,[13,14] similar to the Mott physics of high T_c superconductors. The existence of a layered antiferromagnetic state is supported by the most recent experiment with high quality samples,[7] which feature completely insulating behavior at the charge neutrality point.

There is, so far, no systematic study of superconducting instabilities in the presence of electron-electron and electron-phonon interactions on the honeycomb bilayer at finite doping (see, however, Ref. 21 for fermions in the presence of weak electron-electron interactions only at zero chemical potential). To address this question, we study in the present paper a microscopic model of a single effective honeycomb monolayer with reduced nearest-neighbor hopping and third-neighbor hopping, in addition to intersite attractive interactions. The kinetic term of the effective model is obtained by integrating out the "high-energy" degrees of freedom from the direct interlayer hopping (i.e., assuming strong interlayer hopping in the honeycomb bilayer), and the intersite superexchange interaction originates from the Hubbard on-site repulsion. This model is to a certain degree biased to antiferromagnetism and d-wave superconductivity but preserves the usual low-energy description of the bilayer graphene.[20] Moreover, in contrast to the usual low-energy model of bilayer graphene, the present model accounts for the lattice symmetry of the original model (the honeycomb bilayer) that may be relevant for the symmetry of the superconducting order parameters.

Our primary interest here is to find the most probable symmetry of a superconducting instability on the honeycomb bilayer together with an understanding of its nature, i.e., whether this instability is topological. We also aim at an understanding of the change in the superconducting order parameter and correlations as we go from a monolayer to a few-layer honeycomb lattice. The mean-field solution of the introduced model yields a time-reversal symmetry-breaking $d+id$-wave superconducting state at weak coupling, which continuously transforms into a $d_{x^2-y^2}$-wave type with increasing interaction. Near $3/8$ and $5/8$ filling of the π bands, i.e., near the Van Hove singularity in the density of states, the Cooper pairing becomes much stronger. Our conclusion is that the $d+id$ superconducting instability is the leading superconducting instability of the honeycomb bilayer with strong interlayer hopping at finite doping, and the same instability may be present in the bilayer graphene at finite doping. However, due to the presumed smallness of the coupling constant and order parameter, as well as strong quantum fluctuations in two dimensions, it may be difficult to detect this order experimentally in today's graphene samples.

The remaining part of the paper is organized as follows. In Sec. II we define our effective two-band model on an effective

honeycomb lattice with third-nearest-neighbor hopping. The model is then, in Sec. III, solved by a Bogoliubov-de Gennes (BdG) transformation for a singlet bond-pairing order parameter, and we discuss the relevant symmetries. Section IV presents the phase diagram obtained from a numerical solution of the BdG equations. In Sec. V, the relevance for the physics of the bilayer graphene is discussed, and our main conclusions are presented in Sec. VI. Two appendices summarize analytically obtained solutions in the weak-coupling BCS limit.

II. MODEL

The honeycomb bilayer lattice consists of two Bernal stacked honeycomb lattices, each consisting of two triangular sublattices as illustrated in Fig. 1 such that the unit cell contains four lattice sites. The Hamiltonian of free electrons on such a lattice is given by

$$\begin{aligned} H_0 = &-t\sum_{\vec{j},\sigma}\sum_{\vec{u}}(a^{\dagger}_{1,\vec{j},\sigma}b_{1,\vec{j}+\vec{u},\sigma} + a^{\dagger}_{2,\vec{j},\sigma}b_{2,\vec{j}-\vec{u},\sigma} + \text{H.c.}) \\ &- t_{\perp}\sum_{\vec{j},\sigma}(a^{\dagger}_{1,\vec{j},\sigma}a_{2,\vec{j},\sigma} + \text{H.c.}) \\ &- \mu\sum_{i,\vec{j}}(a^{\dagger}_{i,\vec{j},\sigma}a_{i,\vec{j},\sigma} + b^{\dagger}_{i,\vec{j},\sigma}b_{i,\vec{j},\sigma}). \end{aligned} \tag{1}$$

Here, the index $i = 1,2$ denotes the layer and $\vec{j}$ enumerates primitive cells. The sum runs over $\vec{u} = \vec{u}_0, \vec{u}_1, \vec{u}_2$, where

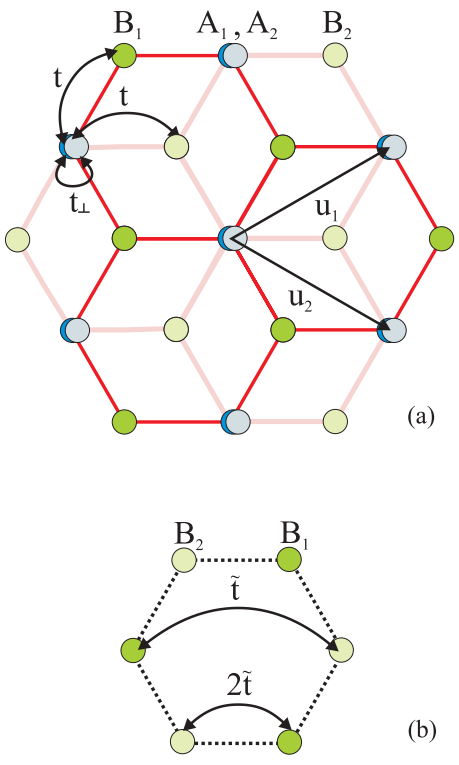

FIG. 1. (Color online) (a) View of Bernal stacked honeycomb lattices 1 and 2 with corresponding sublattice sites A1, B1 and A2, B2, respectively. (b) Model reduced to a monolayer model with the third-neighbor hopping $\tilde{t} \equiv t^2/t_{\perp}$ and the nearest-neighbor hopping $2\tilde{t}$ (see the text).

$\vec{u}_1 = a(\frac{3}{2}, \frac{\sqrt{3}}{2})$ and $\vec{u}_2 = a(\frac{3}{2}, -\frac{\sqrt{3}}{2})$ are the primitive vectors of the lattice, and $\vec{u}_0 = (0, 0)$ is an auxiliary vector for denoting the hopping between sites in the same primitive cell. The norm of these vectors is $|\vec{u}| = \sqrt{3}a$, in terms of the distance a between neighboring sites in each layer, and t is the associated hopping energy, whereas $t_{\perp}$ denotes the interlayer hopping energy between A sites in two different layers. The finite chemical potential μ takes into account doping, either due to the electric-field effect or to chemically active adatoms. The operators $a^{\dagger}_{i,\vec{n},\sigma}(a_{i,\vec{n},\sigma})$ represent electron creation (annihilation) on the sublattice site A_i of the layer i with spin $\sigma = \uparrow, \downarrow$, and $b^{\dagger}_{i,\vec{n},\sigma}(b_{i,\vec{n},\sigma})$ represent those for electrons on the sublattice site B_i. μ is the chemical potential. We use units such that $\hbar = 1$.

By introducing the Fourier transforms $a_{i,\vec{k},\sigma} = \sum_{\vec{j}} a_{i,\vec{j},\sigma}\exp(i\vec{k}\cdot\vec{j})$ and $b_{i,\vec{k},\sigma} = \sum_{\vec{j}} b_{i,\vec{j},\sigma}\exp(i\vec{k}\cdot\vec{j})$, and diagonalizing the Hamiltonian one obtains the spectrum

$$E^{\pm}_{\alpha}(\vec{k}) = \pm\left[(-1)^{\alpha}\frac{t_{\perp}}{2} + \sqrt{\frac{t_{\perp}^2}{4} + t^2|\gamma_{\vec{k}}|^2}\right], \tag{2}$$

where $\alpha = 1,2$, and $\pm$ denote four different branches of dispersion and

$$\gamma_{\vec{k}} = \sum_{\vec{u}} e^{i\vec{k}\cdot\vec{u}} = 1 + e^{i\vec{k}\cdot\vec{u}_1} + e^{i\vec{k}\cdot\vec{u}_2}. \tag{3}$$

In their original work,[20] McCann and Falko showed that the four-band model may be simplified to an effective two-band model if one considers energies much smaller than $t_{\perp}$. In momentum space, the Hamiltonian in Eq. (1) becomes

$$H_0 = \sum_{\sigma}\int_{\text{BZ}}\frac{d^2\vec{k}}{(2\pi)^2} \tag{4}$$

$$\begin{aligned} \{&-t(\gamma_{\vec{k}}a^{\dagger}_{1,\sigma,\vec{k}}b_{1,\sigma,\vec{k}} + \gamma^{*}_{\vec{k}}a^{\dagger}_{2,\sigma,\vec{k}}b_{2,\sigma,\vec{k}} + \text{H.c.}) \\ &- t_{\perp}(a^{\dagger}_{1,\sigma,\vec{k}}a_{2,\sigma,\vec{k}} + \text{H.c.}) - \mu(a^{\dagger}_{1,\sigma,\vec{k}}a_{1,\sigma,\vec{k}} + a^{\dagger}_{2,\sigma,\vec{k}}a_{2,\sigma,\vec{k}} \\ &+ b^{\dagger}_{1,\sigma,\vec{k}}b_{1,\sigma,\vec{k}} + b^{\dagger}_{2,\sigma,\vec{k}}b_{2,\sigma,\vec{k}})\}. \end{aligned} \tag{5}$$

If we introduce the spinor

$$\Psi_{\sigma}(\vec{k}) = (a_{1,\sigma,\vec{k}}, a_{2,\sigma,\vec{k}}, b_{2,\sigma,\vec{k}}, b_{1,\sigma,\vec{k}})^{T}, \tag{6}$$

the Hamiltonian can be expressed as a 4×4 matrix:

$$H_0(\vec{k}) = \sum_{\sigma}\Psi^{\dagger}_{\sigma}(\vec{k})\begin{bmatrix} -\mu & -t_{\perp} & 0 & -t\gamma_{\vec{k}} \\ -t_{\perp} & -\mu & -t\gamma^{*}_{\vec{k}} & 0 \\ 0 & -t\gamma_{\vec{k}} & -\mu & 0 \\ -t\gamma^{*}_{\vec{k}} & 0 & 0 & -\mu \end{bmatrix}\Psi_{\sigma}(\vec{k}). \tag{7}$$

One may further define 2×2 matrices $H_{11} = -\mu I + t_{\perp}\sigma_x$, $H_{22} = -\mu I$, and $H_{12} = -t(\text{Re}\,\gamma_{\vec{k}}\sigma_x + \text{Im}\,\gamma_{\vec{k}}\sigma_y) = H_{21}$, such that the eigenvalue equation can be written in the following form ($\vec{k}$ indices are implied):

$$\begin{bmatrix} H_{11} & H_{12} \\ H_{21} & H_{22} \end{bmatrix}\begin{bmatrix} \Psi_1 \\ \Psi_2 \end{bmatrix} = E\begin{bmatrix} \Psi_1 \\ \Psi_2 \end{bmatrix}, \tag{8}$$

from which we obtain

$$\{H_{22} - H_{21}(H_{11} - E)^{-1}H_{12}\}\Psi_2 = E\Psi_2. \tag{9}$$

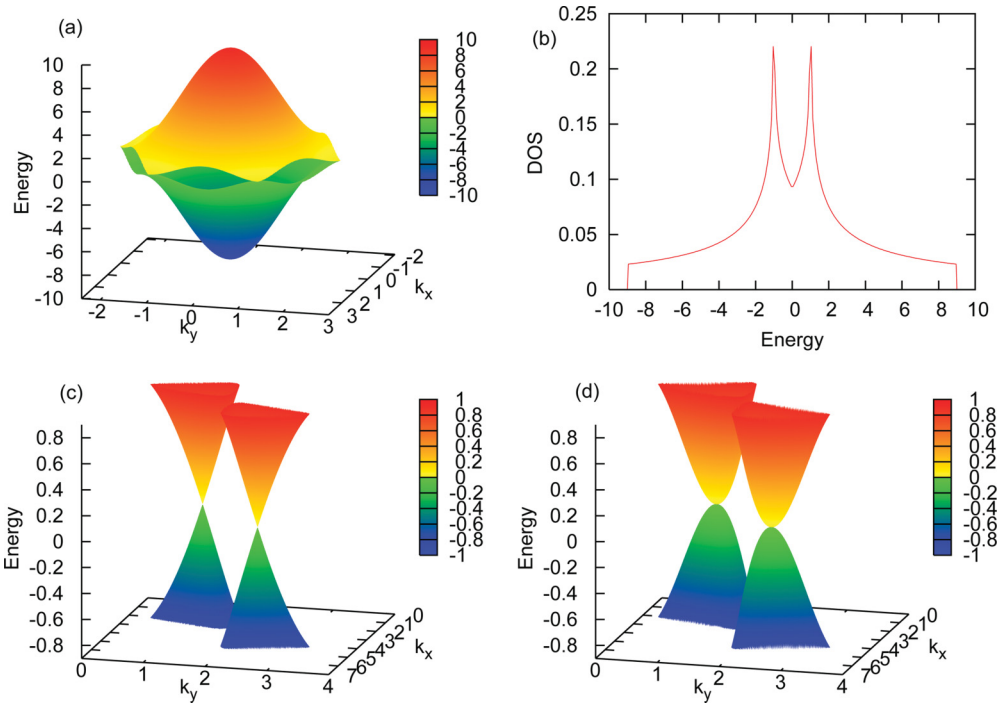

FIG. 2. (Color online) (a) Noninteracting dispersion and (b) density of states of the projected monolayer model. (c) Linear dispersion in the vicinity of the K points in the graphene monolayer in comparison to (d) quadratic dispersion in our model. We use $\tilde{t} = t^2/t_\perp$ for the unit of energy.

If we assume $t_\perp$ to be the largest-energy scale and consider the low-energy limit ($E \ll t_\perp$), Eq. (9) becomes

$$H_{\text{eff}}\Psi_2 \equiv \begin{bmatrix} -\mu & \frac{t^2}{t_\perp}\gamma_{\vec{k}}^2 \\ \frac{t^2}{t_\perp}\gamma_{\vec{k}}^{*2} & -\mu \end{bmatrix} \Psi_2 = E\Psi_2, \qquad (10)$$

with $\Psi_2(\vec{k}) = (b_{2,\sigma,\vec{k}}, b_{1,\sigma,\vec{k}})^T$.

The two-band model described by the Hamiltonian in Eq. (10) is also valid in the limit[20] where $E \ll t_\perp \ll t$. For energies larger than $t_\perp$, one needs to take into account the other two bands which overlap in energy with those considered in Eq. (10). In the following sections we use the simplified two-band model at even larger energies, up to the Van Hove singularity. Formally, this amounts to increasing artificially (with respect to the graphene bilayer) the interlayer hopping $t_\perp$ such that it becomes the largest-energy scale, $t_\perp \gg t$. In that limit Eq. (10) becomes the exact description of the honeycomb bilayer for $E, t \ll t_\perp$ and for the wave vectors of the whole Brillouin zone. We will adopt that model in the following.

The Hamiltonian in Eq. (10) corresponds, in real space, to a single-layer honeycomb lattice with nearest-neighbor and third-neighbor hoppings. Whereas the effective hopping amplitude of the latter is given by $t^2/t_\perp$, the effective nearest-neighbor hopping is twice as large.[23] This means that due to the strong interlayer hopping the complete low-energy physics is projected onto the B1 and B2 sublattices, which themselves form a hexagonal lattice (see Fig. 1).

As mentioned above, the model is equivalent to the graphene bilayer in the small-momentum limit, i.e., for $t^2/t_\perp|ka|^2 \sim \mu \ll t^2/t_\perp$, and reproduces correctly the finite density of states (DOS) at $E = 0$ of bilayer graphene (Fig. 2). Finally, the Hamiltonian in Eq. (10) does not take into account direct hopping between the B1 and B2 sublattices, which may, though, easily be accounted for by adding $-t'\gamma_{\vec{k}}^*$ to the off-diagonal matrix elements, where $t' \simeq 0.3$ eV is the associated hopping amplitude. This term yields the so-called trigonal warping close to the charge neutrality point, which consists of a splitting of the parabolic band-contact point into four linear Dirac points.[20] However, these Dirac points are present only at very low energies, for chemical potentials $|\mu|$ in the meV range, such that the parabolic band approximation becomes valid even at low dopings. Since we are interested, here, in moderate doping, we neglect this additional term and use the effective band the model in Eq. (10) in the following sections.

Since we consider the effective hopping $t^2/t_\perp$ to be small, and if there is a significant on-site repulsion U, spin-singlet bonds between B1 and B2 sites are expected to form due to superexchange processes. Therefore, we apply the $t - J$ model but relax the requirement of the model that double occupation of sites is excluded. We justify this by our primary aim: to find the most probable symmetry of the superconducting instability. As we will be working in the mean-field approximation, we just assume an effective nearest-neighbor attractive interaction between electrons on B1 and B2 sublattices, and in doing this we favor spin-singlet bond formation. The spin-singlet formation directly follows from the mean-field approach to the $t - J$ model.[22] If the attractive interaction is not too strong, it can be simply added to Hamiltonian Eq. (10), with the help of the term

$$H_I = -J \sum_{\vec{j},\vec{u}} \sum_{\sigma} b^\dagger_{1,\vec{j},\sigma} b_{1,\vec{j},\sigma} b^\dagger_{2,\vec{j}+\vec{u},-\sigma} b_{2,\vec{j}+\vec{u},-\sigma}, \qquad (11)$$

where $J > 0$. Now we apply the BCS ansatz by introducing the superconducting order parameter as a three component complex vector:

$$\Delta \equiv (\Delta_{\vec{u}_0}, \Delta_{\vec{u}_1}, \Delta_{\vec{u}_2}),$$

where the components are defined by

$$\Delta_{\vec{u}} = \frac{1}{\sqrt{2}} \langle b_{1,\vec{j},\uparrow} b_{2,\vec{j}+\vec{u},\downarrow} - b_{1,\vec{j},\downarrow} b_{2,\vec{j}+\vec{u},\uparrow} \rangle \tag{12}$$

and correspond to the spin-singlet pairing amplitudes of three inequivalent pairs of nearest neighbors. The interaction part H_I in the mean-field approximation becomes

$$H_{\mathrm{BCS}} = \sqrt{2} J \sum_{\vec{j},\vec{u}} \Delta_{\vec{u}} (b^\dagger_{1,\vec{u},\uparrow} b^\dagger_{2,\vec{j}+\vec{u},\downarrow} - b^\dagger_{1,\vec{j},\downarrow} b^\dagger_{2,\vec{j}+\vec{u},\uparrow}) + \mathrm{H.c.} + 2N \sum_{\vec{u}} J |\Delta_{\vec{u}}|^2, \tag{13}$$

where N is the number of unit cells.

III. BOGOLIUBOV-DE GENNES ANALYSIS AND PAIRING SYMMETRIES

The complete BCS Hamiltonian in momentum space is given by

$$H = -\frac{t^2}{t_\perp} \sum_{\vec{k},\sigma} \left(\gamma^2_{\vec{k}} b^\dagger_{2,\vec{k}\sigma} b_{1,\vec{k}\sigma} + \mathrm{H.c.} \right) + \sqrt{2} J \sum_{\vec{k}} \left[\sum_{\vec{u}} \Delta_{\vec{u}} e^{i\vec{k}\cdot\vec{u}} (b^\dagger_{2,\vec{k}\uparrow} b^\dagger_{1,-\vec{k}\downarrow} - b^\dagger_{2,\vec{k}\downarrow} b^\dagger_{1,-\vec{k}\uparrow}) + \mathrm{H.c.} \right] - \mu \sum_{\vec{k},\sigma} (b^\dagger_{1,\vec{k}\sigma} b_{1,\vec{k}\sigma} + b^\dagger_{2,\vec{k}\sigma} b_{2,\vec{k}\sigma}). \tag{14}$$

Similar to the case of the honeycomb monolayer,[22] we can make our description much more transparent if we apply the following transformation that diagonalizes the kinetic part of the above Hamiltonian:

$$\begin{bmatrix} b_{2,\vec{k}\sigma} \\ b_{1,\vec{k}\sigma} \end{bmatrix} = \frac{1}{\sqrt{2}} \begin{bmatrix} d_{\vec{k}\sigma} + c_{\vec{k}\sigma} \\ e^{-i2\varphi_{\vec{k}}} (d_{\vec{k}\sigma} - c_{\vec{k}\sigma}) \end{bmatrix}, \tag{15}$$

where $\varphi_{\vec{k}} = \arg(\gamma_{\vec{k}})$.

In this basis, where $c_{\vec{k}\sigma}$ and $d_{\vec{k}\sigma}$ represent the electron states in the upper and lower band, respectively, the Hamiltonian transforms into

$$H = \sum_{\vec{k}} \left\{ \sum_{\sigma} (\tilde{t}\epsilon_{\vec{k}} - \mu) c^\dagger_{\vec{k}\sigma} c_{\vec{k}\sigma} + \sum_{\sigma} (-\tilde{t}\epsilon_{\vec{k}} - \mu) d^\dagger_{\vec{k}\sigma} d_{\vec{k}\sigma} + \sqrt{2} J \left[\sum_{\vec{u}} \Delta_{\vec{u}} \cos(\vec{k}\cdot\vec{u} - 2\varphi_{\vec{k}}) (d^\dagger_{\vec{k}\uparrow} d^\dagger_{-\vec{k}\downarrow} - c^\dagger_{\vec{k}\uparrow} c^\dagger_{-\vec{k}\downarrow}) + \sum_{\vec{u}} i \Delta_{\vec{u}} \sin(\vec{k}\cdot\vec{u} - 2\varphi_{\vec{k}}) (c^\dagger_{\vec{k}\uparrow} d^\dagger_{-\vec{k}\downarrow} - d^\dagger_{\vec{k}\uparrow} c^\dagger_{-\vec{k}\downarrow}) \right] + \mathrm{H.c.} \right\}. \tag{16}$$

Here $\tilde{t} \equiv t^2/t_\perp$ and $\epsilon_{\vec{k}} \equiv |\gamma_{\vec{k}}|^2$. The eigenvalues are given by

$$E_{\vec{k}} = \pm \sqrt{(\tilde{t}\epsilon_{\vec{k}})^2 + \mu^2 + 2J^2(|S_{\vec{k}}|^2 + |C_{\vec{k}}|^2) \pm 2\sqrt{A}}, \tag{17}$$

where $C_{\vec{k}} = \sum_{\vec{u}} \Delta_{\vec{u}} \cos(\vec{k}\cdot\vec{u} - 2\varphi_{\vec{k}})$, $S_{\vec{k}} = \sum_{\vec{u}} \Delta_{\vec{u}} \sin(\vec{k}\cdot\vec{u} - 2\varphi_{\vec{k}})$, and

$$A = (\mu^2 + 2J^2|S_{\vec{k}}|^2)\tilde{t}^2\epsilon^2_{\vec{k}} + 4J^4(\mathrm{Re}C_{\vec{k}}\mathrm{Im}S_{\vec{k}} - \mathrm{Im}C_{\vec{k}}\mathrm{Re}S_{\vec{k}})^2. \tag{18}$$

If all $\Delta_{\vec{u}}$ are purely real, i.e., there is no time-reversal symmetry breaking, then the second term in A is zero and the expression for the dispersion simplifies to

$$E_{\vec{k}} = \pm \sqrt{\left(\tilde{t}\epsilon_{\vec{k}} \pm \sqrt{\mu^2 + 2J^2 S^2_{\vec{k}}}\right)^2 + 2J^2 C^2_{\vec{k}}}. \tag{19}$$

In this case $S_{\vec{k}}$ only renormalizes the chemical potential, whereas $C_{\vec{k}}$ plays the main role in the description of the superconducting order parameter. A comparison between the Bogoliubov energy dispersion in Eq. (19) and the usual BCS expression shows that $C_{\vec{k}}$ can be identified with the gap function. However, this name may be misleading because $C_{\vec{k}}$ does not describe the gap, as in the example in Eq. (22) below.

The symmetry analysis of the order parameter on a honeycomb lattice[22] yields the basis vectors which correspond to s, $d_{x^2-y^2}$, and d_{xy} waves, respectively:

$$\Delta = \begin{cases} \Delta\,(1, & 1, & 1) \\ \Delta\,(2, & -1, & -1) \\ \Delta\,(0, & 1, & -1) \end{cases}. \tag{20}$$

The function $C_{\vec{k}}$ corresponding to these symmetries is shown in Fig. 3, in comparison with the monolayer case. The last two possibilities belong to a two-dimensional (2D) subspace of irreducible representation of permutation group $\mathcal{S}_3$.[24] This means that any superposition of these two order parameters, which we may identify with the $d_{x^2-y^2}$ [$(2,-1,-1)$ of Eq. (20) and permutations] and d_{xy} [$(0,1,-1)$ of Eq. (20) and permutations] solutions of d-wave superconductivity, is possible from a symmetry point of view. In spite of this principle possibility, the precise realization of a particular order parameter is a question of energy calculations. One notices that the spatial

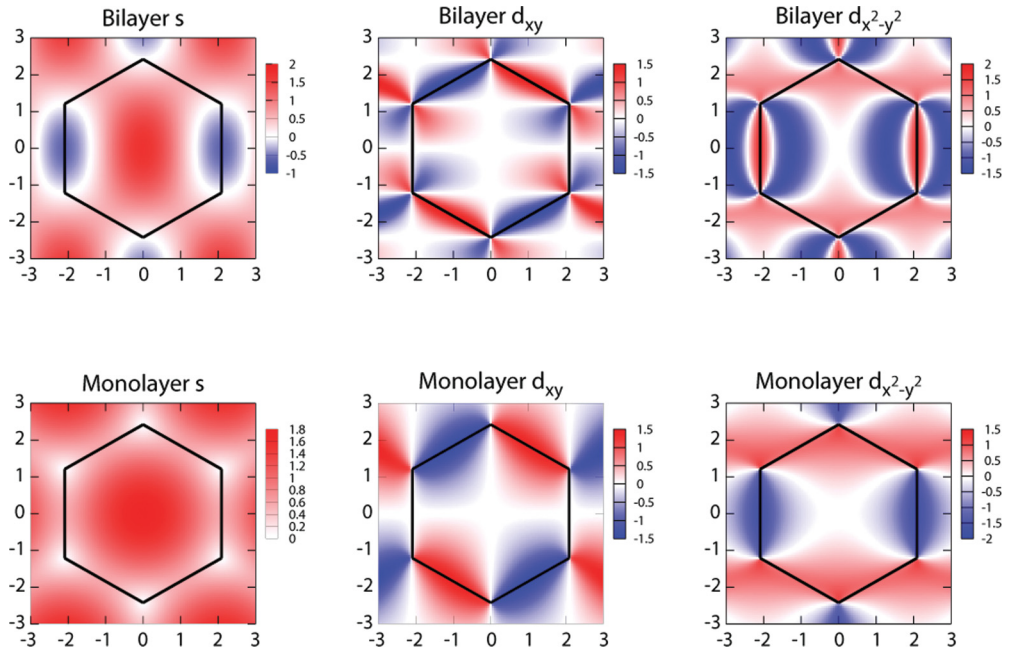

FIG. 3. (Color online) C_k in the first Brillouin zone calculated for three possible symmetries on monolayer and projected bilayer lattices.

point symmetry of the underlying honeycomb lattice is C_{3v}, which includes $2\pi/3$ rotations, whereas a transformation from $d_{x^2-y^2}$ to d_{xy} involves $\pi/4$ rotations. The order parameters thus have a different symmetry than the underlying lattice, as one may also see in Fig. 3, such that the two order parameters do not represent degenerate ground states. Indeed we find, within the BCS mean-field theory, that the $d_{x^2-y^2}$ solution has a lower energy than the d_{xy} solution.

This finding needs to be contrasted to the case of p-wave superconductivity on the square lattice.[31] In the latter case, superpositions of the p_x and p_y solutions are also permitted by the symmetry of the order parameter, but both solutions are related to each other by $\pi/2$ rotations that respect the point symmetry of the underlying (square) lattice. The p_x and p_y solutions are therefore degenerate.

The above arguments indicate that the C_{3v} symmetry of the honeycomb lattice is dynamically broken, only through interactions, via the formation of a $d_{x^2-y^2}$ order parameter. This is similar to the findings of Poletti *et al.* in the context of superfluidity of spinless fermions with nearest-neighbor attraction.[24] Also in this case, the C_{3v} symmetry is dynamically broken. Notice finally that in the small-J limit, i.e., at weak coupling or in the low-energy limit, the BdG system recovers the symmetry of the C_{3v} group but has also an (emergent) continuous rotational symmetry that will lead to a $d_{x^2-y^2} \pm i\sqrt{3}\, d_{xy}$ instability (see Appendix A).

In the case of an s-wave order parameter with $\Delta = \Delta\,(1,1,1)$, a small-wave-vector expansion ($|\vec{q}|a \ll 1$) around the K points yields

$$C_{\vec{K}_\pm+\vec{q}} \approx \mp\frac{\sqrt{3}}{2} q_y a\Delta, \qquad S_{\vec{K}_\pm+\vec{q}} \approx +\frac{\sqrt{3}}{2} q_x a\Delta. \tag{21}$$

Thus both couplings are nonzero and no simple effective picture emerges by looking at the Hamiltonian in Eq. (16). The lower excitation energy branch can be approximated in the small-momentum limit as

$$\begin{aligned} E_{\vec{q}} &\simeq \sqrt{\mu^2 - 2\mu\tilde{t}\epsilon_{\vec{K}_\pm+\vec{q}} + \tfrac{3}{2}J^2(|\vec{q}|a)^2\Delta^2} \\ &\simeq \sqrt{\mu^2 - \tfrac{3}{2}[3\mu\tilde{t} - (J\Delta)^2](|\vec{q}|a)^2}, \end{aligned} \tag{22}$$

where we have used $\epsilon_{\vec{K}_\pm+\vec{q}} \simeq 9(|\vec{q}|a)^2/4$.

If the coupling strengths are such that $E_{\vec{q}}$ has a minimum at $q = 0$, that is for $(J\Delta)^2 > 3\mu\tilde{t}$, a special superconducting instability may be realized (if other possibilities, order parameters, have higher free energy).[25] In the absence of trigonal warping at very low doping, we obtain a time-reversal invariant superconducting instability with two kinds of Cooper pairs with $p_x + ip_y$ and $p_x - ip_y$ pairings. Due to the forms of $C_{\vec{k}}$ and $S_{\vec{k}}$ in the above Hamiltonian in the small-momentum limit, p-wave Cooper pairings are expected. For a sufficiently large chemical potential, one can neglect $S_{\vec{k}}$ in Eq. (19) and the system may be unstable towards a p_y gapless superconductor, with gap minima on the Fermi surface, i.e., on a circle.

For $\Delta = \Delta(2,-1,-1)$, the small-momentum expansion around the K points yields

$$\begin{aligned} C_{\vec{K}_\pm+\vec{q}}(d_{x^2-y^2}) &\approx -3\frac{(q_x^2 - q_y^2)}{|\vec{q}|^2}\Delta, \\ S_{\vec{K}_\pm+\vec{q}}(d_{x^2-y^2}) &\approx \mp 6\frac{q_x q_y}{|\vec{q}|^2}\Delta \end{aligned} \tag{23}$$

and for $\Delta = \Delta(0,1,-1)$

$$\begin{aligned} C_{\vec{K}_\pm+\vec{q}}(d_{xy}) &\approx 2\sqrt{3}\frac{q_x q_y}{|\vec{q}|^2}\Delta, \\ S_{\vec{K}_\pm+\vec{q}}(d_{xy}) &\approx \mp\sqrt{3}\frac{(q_x^2 - q_y^2)}{|\vec{q}|^2}\Delta. \end{aligned} \tag{24}$$

The gap function $C_{\vec{k}}$ thus clearly shows the $d_{x^2-y^2}$ and the d_{xy} symmetry in Eqs. (23) and (24), respectively.

Notice that one may superpose two waves in the manner

$$C_{\vec{k}}(d \pm id) = C_{\vec{k}}(d_{x^2-y^2}) \pm i\sqrt{3}C_{\vec{k}}(d_{xy}) \tag{25}$$

and

$$S_{\vec{k}}(d \pm id) = S_{\vec{k}}(d_{x^2-y^2}) \pm i\sqrt{3}S_{\vec{k}}(d_{xy}), \tag{26}$$

which is identified with the $d + id$-wave superconducting phase in the following. In the small-wave-vector limit, the combined forms of $C_{\vec{k}}$,

$$C_{\vec{K}_\pm+\vec{q}}(d + id) \approx \mp iS_{\vec{K}_\pm+\vec{q}} \approx 3(q_x + iq_y)^2/|\vec{q}|^2 \tag{27}$$

and

$$C_{\vec{K}_\pm+\vec{q}}(d - id) \approx \pm iS_{\vec{K}_\pm+\vec{q}} \approx 3(q_x - iq_y)^2/|\vec{q}|^2, \tag{28}$$

restore the rotational symmetry—they are indeed eigenstates of rotation in two dimensions with the value of angular momentum equal to 2. Thus a fixed complex combination in real space, either $d_{x^2-y^2} + i\sqrt{3}\, d_{xy}$ or $d_{x^2-y^2} - i\sqrt{3}\, d_{xy}$, leads to the same form of the expansion in small momenta at both valley points, either Eq. (27) or Eq. (28). Because it is the same irrespective of the valley K or K' one obtains a solution that spontaneously breaks time-reversal symmetry. Thus we can identify the solution with the broken time-reversal symmetry $d + id$ state. Something similar happens in the monolayer case, but the d-wave symmetry is recognized as a global dependence of the order parameter on the $\vec{k}$ vector in the Brillouin zone around the central Γ point (see Ref. 26) and p-wave behavior around $\vec{K}_\pm$ points.[27] In the bilayer case the time-reversal symmetry breaking d-wave order parameter emerges as a property of the low-energy small-momentum effective description around the K points, as shown above.

IV. PHASE DIAGRAM

We have found the ground state of our model Hamiltonian for a broad range of J and μ by minimizing the free energy. At zero temperature, as a function of the order parameter, it is given by

$$F = -\sum_{\vec{k}\in \mathrm{IBZ}} \sum_{\alpha=\pm1} E_{\vec{k},\alpha} + 2NJ \sum_{\vec{u}} |\Delta_{\vec{u}}|^2, \tag{29}$$

where the first sum is over all wave vectors $\vec{k}$ in the first Brillouin zone and two Bogoliubov bands with positive energies. The ground state is defined as a global minimum of the free energy in the order-parameter space. In the present study, we concentrate on superconducting order parameters in a variational approach, and thus we cannot exclude that other correlated (nonsuperconducting) phases may have an even lower energy. In the mean-field approach, superconducting ground states are expected even for infinitesimal positive values of J.

The order-parameter space is six-dimensional, because it is defined by three complex numbers. However, adding the same phase to all three complex parameters does not modify the physical state, so one can always make one of the parameters purely real (we set $\Delta_{d_{x^2-y^2}}$ real) and reduce the order-parameter space dimensionality to 5. We used the amoeba numerical method[28] to directly minimize the free energy. Five-dimensional minimization often reveals more than one local minimum, but we were always able to identify the lowest-lying state to a satisfying level of certainty. However, for small values of J, the local free-energy minima are extremely shallow, with energies only slightly lower than the free energy of the normal state. Such features in the free-energy landscape are completely clouded by numerical noise due to the discretization of the first Brillouin zone. Our numerical calculations are therefore limited to higher values of J, which give a solution with the amplitude of the order parameter larger than 10^{-4}. This is marked by the dashed lines in Fig. 4.

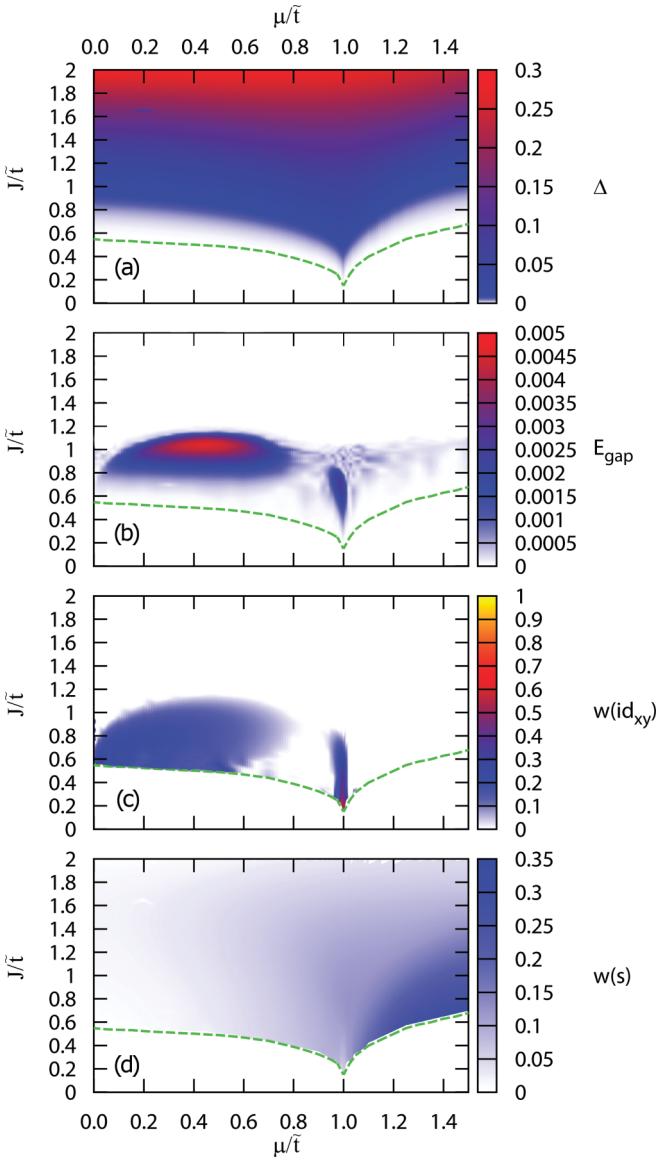

FIG. 4. (Color online) (a) Order-parameter amplitude Δ in the (μ, J) parameter space, obtained by a minimization of the free energy, (b) single-particle excitation gap, (c) contribution of id_{xy}, and (d) s-wave component in the ground-state order parameter. The green dashed line marks where Δ drops below 10^{-4}. Below this line, our numerics is not reliable. We use $\tilde{t} = t^2/t_\perp$ for the unit of energy.

Our results are shown on Fig. 4, where the relevant quantities are represented by color in the (μ, J) plane. The amplitude of the order parameter is shown in Fig. 5(a).

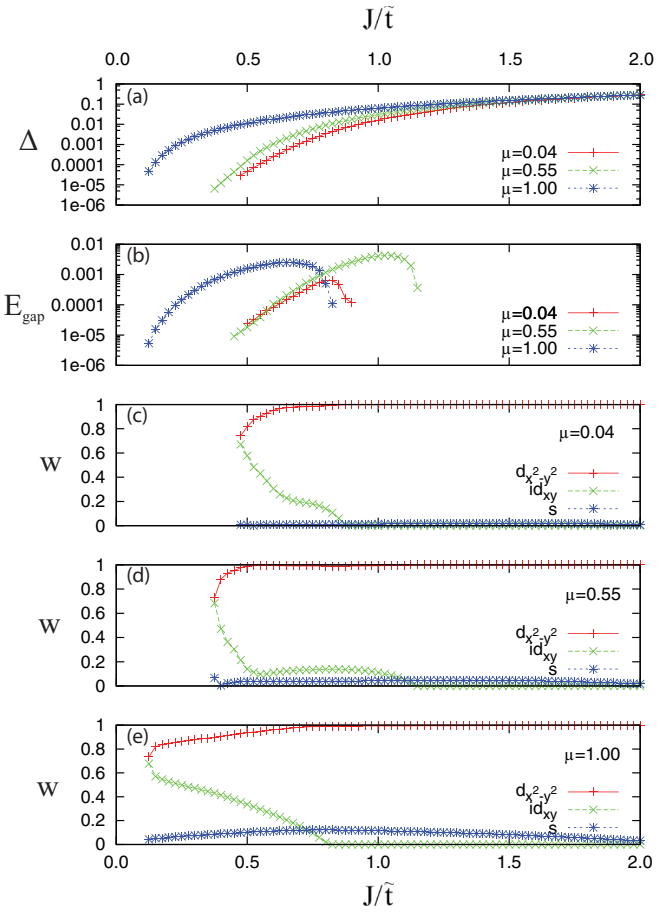

FIG. 5. (Color online) (a) Order-parameter amplitude Δ and (b) single-particle excitation gap as a function of J, for $\mu = 0.04, 0.55, 1$. (c–e) The contributions of three relevant symmetry components. The $d_{x^2-y^2}$ component is the dominant one for large J. The contribution of id_{xy} increases with decreasing J until the two contributions are equal and we find a pure $d+id$-wave symmetry. We use $\tilde{t} = t^2/t_\perp$ for the unit of energy. The data are plotted only above the value for the coupling J which is numerically significant, as mentioned in the text (see also the dashed green line in Fig. 4).

Upon small to moderate doping, the SC instability increases and becomes particularly favorable at the filling 5/8, which corresponds to the chemical potential $\mu/\tilde{t} = 1$, and the Van Hove singularity in the noninteracting DOS. For further doping the SC instability decreases. This gives to Fig. 4(a) roughly the look of the inverse DOS of Fig. 2(b). The gap in the single-particle excitations is shown in Fig. 4(b). It is particularly pronounced in the case of strong mixing of $d_{x^2-y^2}$ and id_{xy} symmetry components, as we can see from Fig. 4(c). The contribution of different pairing symmetries is defined by the ratio w of different components of Δ, where

$$\mathbf{\Delta} = \Delta_s \hat{e}_s + i\Delta_{is}\hat{e}_s + \Delta_{d_{xy}}\hat{e}_{d_{xy}} + i\Delta_{id_{xy}}\hat{e}_{d_{xy}} + \Delta_{d_{x^2-y^2}}\hat{e}_{d_{x^2-y^2}}, \tag{30}$$

with $\hat{e}_s = (1,1,1)/\sqrt{3}$, $\hat{e}_{d_{xy}} = (0,1,-1)/\sqrt{2}$, and $\hat{e}_{d_{x^2-y^2}} = (2,-1,-1)/\sqrt{6}$. Figure 4(c) shows the ratio $w(id_{xy}) = |\Delta_{id_{xy}}|/|\Delta|$, and Fig. 4(d) shows the ratio $w(s) = |\Delta_s|/|\Delta|$. The contributions of is and d_{xy} components are negligible in all cases, and $d_{x^2-y^2}$ is the dominant component.

The numerical results are, for clarity, also shown in Fig. 5 for three chosen values of the chemical potential, $\mu/\tilde{t} = 0.04, 0.55, 1$. Figure 5(a) shows a sudden increase in the pairing amplitude with the increasing interaction J (note the logarithmic scale on the y axis). For small J, the pairing amplitude is much larger for $\mu/\tilde{t} = 1$, i.e., at the Van Hove singularity, and in this case the single-particle excitation gap is also larger due to the strong mixing of $d_{x^2-y^2}$ and id_{xy} symmetries. Contributions of relevant components are compared in Figs. 5(c)–5(e). At higher values of J one has a pure $d_{x^2-y^2}$ symmetry, whereas a mixture of $d_{x^2-y^2}$ and id_{xy} symmetries is found at lower values of J. The contribution of id_{xy} symmetry increases with decreasing J, and almost pure $d+id$ symmetries are usually found at the lowest accessible values of J.

Our numerical calculations were performed on processors with 8 GB of RAM, which limited the number of $\vec{k}$ points in the first Brillouin zone to 4000×4000, but we checked that results do not differ qualitatively even with a much sparser 2000×2000 $\vec{k}$ grid. A much denser and probably a nonuniform discretization of the first Brillouin zone would be needed to probe the weak-coupling behavior of our model, that is for values of J below the dashed lines in Fig. 4. Notice, however, that the system in the small-J limit may be treated analytically within the weak-coupling limit, the results of which are presented in Appendices A and B, for the cases of finite and zero chemical potential, respectively.

In this weak-coupling regime and at finite chemical potential, we find that the $d+id$ superconducting order parameter yields the lowest mean-field energy, when compared to order parameters that respect time-reversal symmetry (Appendix A), in agreement with our numerical results for larger values of J. In the weak-coupling limit, in the symmetry-protected subspace of $d_{x^2-y^2}$ and d_{xy} order parameters the complex combination $d_{x^2-y^2} + i\sqrt{3}d_{xy}$ leads to a fully gapped system with no nodes at the Fermi surface. This means that the gap is proportional to $|C_{\vec{k}}| = \text{const}$, and maximum gain in the energy for this superconducting instability is obtained. Notice that this topological instability is in line with a theorem for the BCS description, according to which a time-reversal symmetry-broken 2D superconducting state has a lower free energy, as compared to time-reversal symmetric ones, when confronted with two-dimensional representations of the superconducting order parameter.[31] Indeed, as mentioned after Eq. (20), the $d_{x^2-y^2}$ and d_{xy} components of the order parameter $\mathbf{\Delta}$ form a two-dimensional irreducible representation of the symmetry group of the honeycomb lattice. Although the theorem of Ref. 31 was derived for a single band, it is expected also to apply to the present case at finite doping when the higher Bogoliubov band is irrelevant for the superconducting instability. This instability occurs at any strength of attractive interaction at finite doping since the gap opens as

$$J\Delta \propto \exp\left[-\frac{8\pi}{\sqrt{3}}\frac{1}{\rho(\mu)J}\right] \tag{31}$$

(see Appendix A), in terms of the DOS $\rho(E_F)$ at the Fermi level E_F. This is simply the BCS expression with the pairing potential equal to J.

Finally, we notice that the weak-coupling analysis yields a different picture at zero doping (Appendix B), where a time-reversal-symmetric superconducting order parameter (with any real combination of $d_{x^2-y^2}$ and d_{xy}) is energetically favored.

V. POSSIBLE RELEVANCE FOR BILAYER GRAPHENE

In the following we will discuss the possible relevance of our model for the physics of bilayer graphene. With an estimate[1,29] for the Coulomb on-site repulsion, $U \sim 10$ eV, intralayer nearest-neighbor hopping,[30] $t \sim 3$ eV, and interlayer hopping,[30] $t_\perp \sim 0.4$ eV, bilayer graphene may have a tendency to develop strongly correlated electron phases. Notice that, although similar energy scales are found in monolayer graphene, the latter is to great accuracy described in terms of (quasi-)free electrons because of a vanishing DOS at the Fermi level, in the absence of intensive doping.[1–3] In contrast, electronic correlations are much more efficient in bilayer graphene as a consequence of the finite DOS even at the band-contact points. This finite DOS may also be invoked when considering screening. Whereas screening is highly inefficient in monolayer graphene, and one needs then to take into account the long-range nature of the electronic interaction potential, the screening properties in bilayer graphene are similar to those in usual 2D electron systems with a parabolic band dispersion, albeit with a rather small band mass ($\sim 0.05 m_0$, in terms of the bare electron mass). In this sense, an approach based on the Hubbard model, as used here excluding nearest- and further-neighbor interactions, is better justified in bilayer than in monolayer graphene. However, this remains a strong approximation, as in the case of 2D electrons in GaAs heterostructures, and numerical calculations indicate that longer-range terms remain relevant also in bilayer graphene.[29]

Generally, the interplay between a strong on-site repulsion U and the hopping terms t and $t_\perp$ leads to antiferromagnetic Heisenberg-type exchange interactions, $J \sim t^2/U \sim 1$ eV between nearest neighbors in the same layer and $J_\perp \sim t_\perp^2/U \sim 16$ meV between nearest neighbors in opposite layers. Although clear evidence for antiferromagnetism is lacking in bilayer graphene, the quadratic dispersion of juxtaposed conduction and valence bands (together with the nonzero density of states) favor antiferromagnetic fluctuations.[32] Because the low-energy electrons move preferentially on the B1 and B2 sublattice sites, one needs to estimate an effective exchange interaction between them that may be obtained from a perturbative expansion, $J_{\text{eff}} \sim J^2 J_\perp / t_\perp^2 \sim t^4/U^3 \sim 100$ meV.

Remember that the effective hopping parameter in the projected honeycomb lattice (between the B1 and B2 sites) is a more subtle issue because it is derived in the limit where $t_\perp \gg t$, in contrast to the natural order in bilayer graphene. In order to make a comparison between our effective model and that of bilayer graphene, in view of the correlated phases we consider, it is therefore more appropriate to define the effective hopping indirectly from the value of J_{eff} and U, $J_{\text{eff}} \sim t_{\text{eff}}^2/U$, which yields a value of $t_{\text{eff}} \sim 1$ eV that should replace the value $\tilde{t}$ in the previous sections.

Therefore modeled with two effective parameters, J_{eff} and t_{eff}, bilayer graphene may be compared with the effective honeycomb lattice considered in our paper and the corresponding $t-J$ model. The main feature of bilayer graphene appears to be that $J_{\text{eff}} \sim 0.1 t_{\text{eff}} \ll t_{\text{eff}}$, and in considering the relevance of our model we should confine ourselves to weak couplings and small or moderate dopings; because we simplified the high-momentum physics of the bilayer (by considering the large $t_\perp$ limit) we should confine ourselves to lower dopings. First one sees from Fig. 4 that the gaps are in the meV range (2 to 5 meV for the maximal gaps) if one considers the energy scale $t_{\text{eff}} \sim J \sim 1$ eV. Thus our results indicate very small energy scales that are unlikely to be resolved in today's graphene samples. Furthermore we should use t_{eff} and J_{eff} for t and J for the exponent in the weak-coupling analysis in Appendix A. Because we estimate $t_{\text{eff}}/J_{\text{eff}} \sim 10$, the weak-coupling analysis yields an exponential suppression and gaps below 1 meV, in agreement with our numerical findings shown in Fig. 4.

VI. CONCLUSIONS

We presented an analysis of a model of a honeycomb bilayer with attractive interactions that (1) supports $d+id$ superconductivity with the canonical effective (low-momentum) description $\sim(k_x+ik_y)^2$ at both valley points and (2) transforms at moderate and strong couplings into $d_{x^2-y^2}$ superconductivity. The implied tJ model may be relevant for future investigations of such a complex and intriguing system as the graphene bilayer. We discussed the possibility of a superconducting instability in this framework and concluded that $d+id$ is the leading superconducting instability in the case of the graphene bilayer at moderate dopings and low-energy scales.

We would like to point also to the difference between the monolayer and bilayer case that follows from the symmetry analysis of the simple model with attractive interactions and the ensuing short-range order parameter on both lattices. In the effective description around $\vec{K}$ points an s wave and p wave are found[22,26] in the monolayer case, and a p wave and d wave are found in the bilayer case. The bilayer honeycomb lattice appears at moderate dopings as yet another stage on which time-reversal symmetry-breaking d-wave superconductivity may appear (see Refs. 22,33–37 for moderately doped monolayer) and may be driven by similar physics as in the case of predicted instabilities at special (very high) dopings of a honeycomb monolayer.[38,39] In the case we presented, the canonical[40] low momentum description, $\sim(k_x+ik_y)^2$, holds due to the quadratically dispersing Dirac electrons.

ACKNOWLEDGMENTS

We thank A. M. Black-Schaffer, M. Civelli, M. Franz, and Y. Hatsugai for useful discussions. Furthermore, we thank D. Tanasković for support and his implication at the early stage of this project. J. V. and M. V. M. are supported by the Serbian Ministry of Education and Science under Project No. ON171017, and M. O. G. is supported by the ANR (Agence Nationale de la

Recherche) project NANOSIM GRAPHENE under Grant No. ANR-09-NANO-016. The authors acknowledge financial support from the bilateral MES-CNRS 2011/12 program. This research was funded in part by the NSF under Grant No. NSF PHY05-51164; M. V. M. and M. O. G. acknowledge the hospitality of the Kavli Institute for Theoretical Physics, University of California, Santa Barbara. Numerical simulations were run on the AEGIS e-Infrastructure, supported in part by FP7 projects EGI-InSPIRE, PRACE-1IP, and HP-SEE.

APPENDIX A: WEAK-COUPLING ANALYTICAL SOLUTION AT FINITE CHEMICAL POTENTIAL

Here, we present briefly the weak-coupling analysis of superconducting order in the effective bilayer model. In order to simplify the notation, we use the letter t to denote the effective hopping $\tilde{t}$. The DOS at the Fermi level, $\rho(E_F)$, is on the order of the inverse hopping parameter $1/t$. Notice that if only a parabolic band is taken into account it remains fixed at its $E_F = 0$ value, but corrections to the parabolic approximation immediately yield a contribution that varies linearly with the Fermi level, in agreement with the DOS plotted in Fig. 2(b).

In the case when $\Delta = \Delta(1,1,1)$, a weak-coupling BCS analysis that takes into account only electrons in the lower Bogoliubov band gives

$$J\Delta = \sqrt{2tE_c}\exp\left(-24\sqrt{3}\pi\frac{t}{\mu\rho(E_F)J}\right), \tag{A1}$$

with E_c as an energy cutoff around the Fermi value, for the solution, and

$$\frac{\delta E^p_{\rm MF}}{N} = -(J\Delta)^2\frac{\mu\rho(E_F)}{t}\frac{1}{4\sqrt{3}\pi}, \tag{A2}$$

for the gain in the mean-field energy, $\delta E_{\rm MF}$, by the pairing instability.

The weak-coupling BCS analysis in the case of electron doping ($\mu > 0$) for $d_{x^2-y^2}$ and $d_{x^2-y^2} + i\sqrt{3}\, d_{xy}$ gives

$$J\Delta_d = \frac{\sqrt{2}}{3}E_c\exp\left(-\frac{8\pi}{\sqrt{3}}\frac{1}{\rho(E_F)J} + \frac{1}{2}\right), \tag{A3}$$

for the solution which we denoted by $\Delta = \Delta_d$, and

$$J\Delta = \sqrt{\frac{2}{3}}E_c\exp\left(-\frac{8\pi}{\sqrt{3}}\frac{1}{\rho(E_F)J} + \frac{1}{2}\right), \tag{A4}$$

in the case of the d_{xy} wave. For the energy gain one obtains

$$\frac{\delta E_{\rm MF}(d_{x^2-y^2})}{N} = \frac{\delta E_{\rm MF}(d_{xy})}{N} = -(J\Delta_d)^2\rho(E_F)\frac{3\sqrt{3}}{4\pi}, \tag{A5}$$

and for a $d_{x^2-y^2} + i\sqrt{3}\, d_{xy}$ wave one finds

$$\frac{\delta E^d_{\rm MF}}{N} = -(J\Delta_d)^2\rho(E_F)\frac{3\sqrt{3}}{2\pi}. \tag{A6}$$

Because of its twice lower mean-field energy, the $d_{x^2-y^2} + i\sqrt{3}d_{xy}$ time-reversal symmetry-breaking instability, which we call in short the d wave, is more likely than $d_{x^2-y^2}$- and d_{xy}-wave order parameters. In the large-doping limit, the energy minimization is also much more efficient for the d wave than the p_y wave, as seen in the small value of the ratio

$$\frac{\delta E^p_{\rm MF}}{\delta E^d_{\rm MF}} = \frac{\mu}{2E_c}\exp\left[-\frac{2\pi\times 8}{\sqrt{3}}\frac{1}{\rho(E_F)J}\left(\frac{9t}{2\mu}-1\right)\right], \tag{A7}$$

for $\mu < \frac{9t}{2}$. The most natural choice for E_c is to be of the order of μ as a first energy scale when we start from the smallest one, i.e., J. The time-reversal symmetry-breaking d-wave solution of our BCS mean-field Hamiltonian is also expected from a theorem proved in Ref. 31. The theorem was derived for 2D one-band models that reveal both time-reversal symmetry and a point symmetry described by the dihedral group D_n [or the O(2) rotation symmetry in the case of continuum models]. It states that generally a time-reversal symmetry-breaking superconducting state has a lower free energy than time-reversal symmetric ones if one is confronted with a 2D representation of the symmetry group. In the case of weak coupling that we consider here, i.e., $J \ll \mu$, and $\mu > 0$ (electron doping), we have an effective one-band theory of electrons to which the theorem can be applied. Also, the dispersion of the complex d-wave order parameter is more complicated in our case (than in Ref. 31), as can be seen in Eqs. (17) and (18). But in the weak-coupling limit the J^4 term can be neglected in Eq. (18), and we obtain expressions that are reminiscent of those of Ref. 31.

In the following we investigate more closely an effective low-energy description of the d-wave instability, in the case of high electron doping, and discuss only the lower-energy Bogoliubov band. Therefore our effective Hamiltonian is

$$H_e = \sum_{\vec{k}\sigma}(t\epsilon_{\vec{k}} - \mu)c^\dagger_{\vec{k}\sigma}c_{\vec{k}\sigma} + \sum_{\vec{k}}(\Delta_{\vec{k}}c^\dagger_{\vec{k}\uparrow}c^\dagger_{-\vec{k}\downarrow} + \text{H.c.}), \tag{A8}$$

where $\Delta_{\vec{k}} \sim (k_x - ik_y)^2/|k|^2$. In the weak-coupling BCS analysis it can be easily shown that the Hamiltonian is completely equivalent to the one with $\Delta_{\vec{k}} \sim (k_x - ik_y)^2$, because both Hamiltonians have an effective description on a Fermi circle defined by $t\epsilon_{\vec{k}} = \mu$. With this adjustment we have exactly the form of the BCS Hamiltonian studied in Ref. 40 on time-reversal symmetry-breaking superconductors in two dimensions. In the so-called weak-pairing case for finite $\mu > 0$ that we want to study, the minimum of Bogoliubov excitations moves to finite values of $\vec{k}$, $t\epsilon_{\vec{k}} = \mu$, i.e., to the Fermi surface of free particles. The Cooper pair wave function $g(\vec{r})$ may be a nonuniversal function of $|\vec{r}|$ where $\vec{r}$ is the relative coordinate of the pair. On the other hand, the dependence of the function on the angle of vector $\vec{r}$ is fixed and can easily be derived in the Bogoliubov formalism to be $g(|\vec{r}|) \propto \frac{\bar{z}}{z} \propto (x - iy)^2$ where $z = x + iy$ is the two-dimensional complex coordinate. Thus the relative angular momentum of the Cooper pair is $l = -2$. The weak-pairing phase is topological, gapped in the bulk because $\mu > 0$, and possesses a doublet of spin-1/2 Dirac edge modes.[40] In our case, because of the fermion doubling on the honeycomb lattice and the existence of the two $\vec{K}$ points (valleys) [and because around each one we have the same effective description given by the

Hamiltonian in Eq. (16)], we expect four Dirac modes on the edge.

APPENDIX B: WEAK-COUPLING ANALYTICAL SOLUTION AT ZERO CHEMICAL POTENTIAL

In the weak-coupling limit at $\mu = 0$, when both Bogoliubov bands are taken into account we find for $d_{x^2-y^2}$ symmetry

$$J\Delta^d = \frac{E_c}{3}\exp\left(-\frac{\frac{8}{3J} - 11c}{2c}\right), \tag{B1}$$

with $c \equiv \frac{1}{2\pi\sqrt{3}}\frac{1}{t}$, for the solution, and

$$\frac{\delta E_{\mathrm{MF}}^{d_{x^2-y^2}}}{N} = -\frac{9}{2}c\,(J\Delta^d)^2, \tag{B2}$$

for the energy gain. On the other hand, for $d + id$ symmetry we find

$$J\Delta^{d+id} = \frac{\sqrt{2}E_c}{3}\exp\left(-\frac{\frac{8}{3J} - 5c}{2c}\right), \tag{B3}$$

and

$$\frac{\delta E_{\mathrm{MF}}^{d+id}}{N} = -9c\,(J\Delta^{d+id})^2. \tag{B4}$$

Because

$$\frac{\delta E_{\mathrm{MF}}^{d+id}}{\delta E_{\mathrm{MF}}^{d_{x^2-y^2}}} = \frac{\delta E_{\mathrm{MF}}^{d+id}}{\delta E_{\mathrm{MF}}^{d_{xy}}} = 4e^{-6}, \tag{B5}$$

any real combination of $d_{x^2-y^2}$ and d_{xy} waves is more likely than the $d + id$ wave.

[1] A. H. Castro Neto, F. Guinea, N. M. R. Peres, K. S. Novoselov, and A. K. Geim, Rev. Mod. Phys. **81**, 109 (2009).
[2] V. N. Kotov, B. Uchoa, V. M. Peirera, A. H. Castro Neto, and F. Guinea, Rev. Mod. Phys. **84**, 1067 (2012).
[3] M. O. Goerbig, Rev. Mod. Phys. **83**, 1193 (2011).
[4] J. Martin, B. E. Feldman, R. T. Weitz, M. T. Allen, and A. Yacoby, Phys. Rev. Lett. **105**, 256806 (2010).
[5] R. T. Weitz, M. T. Allen, B. E. Feldman, J. Martin, and A. Yacoby, Science **330**, 812 (2010).
[6] F. Freitag, J. Trbovic, M. Weiss, and C. Schönenberger, Phys. Rev. Lett. **108**, 076602 (2012).
[7] J. Velasco, Jr., L. Jing, W. Bao, Y. Lee, P. Kratz, V. Aji, M. Bockrath, C. N. Lau, C. Varma, R. Stillwell, D. Smirnov, F. Zhang, J. Jung, and A. H. MacDonald, Nature Nanotech. **7**, 156 (2012).
[8] X.-L. Qi and S.-C. Zhang, Rev. Mod. Phys. **83**, 1057 (2011).
[9] H. Min, G. Borghi, M. Polini, and A. H. MacDonald, Phys. Rev. B **77**, 041407(R) (2008).
[10] R. Nandkishore and L. Levitov, Phys. Rev. Lett. **104**, 156803 (2010); Phys. Rev. B **82**, 115124 (2010).
[11] F. Zhang, H. Min, M. Polini, and A. H. MacDonald, Phys. Rev. B **81**, 041402(R) (2010).
[12] O. Vafek and K. Yang, Phys. Rev. B **81**, 041401(R) (2010).
[13] F. Zhang, J. Jung, G. A. Fiete, Q. Niu, and A. H. MacDonald, Phys. Rev. Lett. **106**, 156801 (2011).
[14] J. Jung, F. Zhang, and A. H. MacDonald, Phys. Rev. B **83**, 115408 (2011).
[15] Y. Lemonik, I. L. Aleiner, C. Toke, and V. I. Falko, Phys. Rev. B **82**, 201408 (2010).
[16] F. Zhang and A. H. MacDonald, Phys. Rev. Lett. **108**, 186804 (2012).
[17] R. E. Throckmorton and O. Vafek, Phys. Rev. B **86**, 115447 (2012).
[18] M. Kharitonov, arXiv:1109.1553.
[19] M. M. Scherer, S. Uebelacker, and C. Honercamp, Phys. Rev. B **85**, 235408 (2012).
[20] E. McCann and V. I. Falko, Phys. Rev. Lett. **96**, 086805 (2006).
[21] O. Vafek, Phys. Rev. B **82**, 205106 (2010).
[22] A. M. Black-Schaffer and S. Doniach, Phys. Rev. B **75**, 134512 (2007).
[23] C. Bena and L. Simon, Phys. Rev. B **83**, 115404 (2011).
[24] D. Poletti, C. Miniatura, and B. Gremaud, Europhys. Lett. **93**, 37008 (2011).
[25] Notice that other symmetries of the superconducting order parameter are indeed energetically favored at higher doping, as is shown in the weak-coupling analysis presented in Appendix A.
[26] J. Linder, A. M. Black-Schaffer, T. Yokoyama, S. Doniach, and A. Sudbo, Phys. Rev. B **80**, 094522 (2009).
[27] B. Uchoa and A. H. Castro Neto, Phys. Rev. Lett. **98**, 146801 (2007).
[28] *Numerical Recipes: The Art of Scientific Computing* (Cambridge University Press, Cambridge, 2007).
[29] T. O. Wehling, E. Sasioglu, C. Friedrich, A. I. Lichtenstein, M. I. Katsnelson, and S. Blugel, Phys. Rev. Lett. **106**, 236805 (2011).
[30] K. Zou, X. Hong, and J. Zhu, Phys. Rev. B **84**, 085408 (2011), and references therein.
[31] M. Cheng, K. Sun, V. Galitski, and S. Das Sarma, Phys. Rev. B **81**, 024504 (2010).
[32] A. H. MacDonald, J. Jung, and F. Zhang, Phys. Scr. **146**, 014012 (2012).
[33] G. Baskaran, Phys. Rev. B **65**, 212505 (2002).
[34] C. Honerkamp, Phys. Rev. Lett. **100**, 146404 (2008).
[35] S. Pathak, V. B. Shenoy, and G. Baskaran, Phys. Rev. B **81**, 085431 (2010).
[36] F. M. D. Pellegrino, G. G. N. Angilella, and R. Pucci, Eur. Phys. J. B **76**, 469 (2010).
[37] Z.-C. Gu, H.-C. Jiang, D. N. Sheng, H. Yao, L. Balents, and X.-G. Wen, arXiv:1110.1183.
[38] R. Nandkishore, L. Levitov, and A. Chubukov, Nature Phys. **8**, 158 (2012).
[39] M. Kiesel, Ch. Platt, W. Hanke, D. A. Abanin, and R. Thomale, Phys. Rev. B **86**, 020507(R) (2012).
[40] N. Read and D. Green, Phys. Rev. B **61**, 10267 (2000).